Linear growth of streaming instability in pressure bumps

Jérémy Auffinger, Guillaume Laibe

Monthly Notices
of the
ROYAL ASTRONOMICAL SOCIETY

MNRAS **473,** 796–805 (2018)
Advance Access publication 2017 September 16

doi:10.1093/mnras/stx2395

Linear growth of streaming instability in pressure bumps

Jérémy Auffinger and Guillaume Laibe★

Univ Lyon, Univ Lyon1, Ens de Lyon, CNRS, Centre de Recherche Astrophysique de Lyon UMR5574, F-69230 Saint-Genis-Laval, France

Accepted 2017 September 12. Received 2017 September 12; in original form 2017 July 20

ABSTRACT

Streaming instability is a powerful mechanism which concentrates dust grains in protoplanetary discs, eventually up to the stage where they collapse gravitationally and form planetesimals. Previous studies inferred that it should be ineffective in viscous discs, too efficient in inviscid discs and may not operate in local pressure maxima where solids accumulate. From a linear analysis of stability, we show that streaming instability behaves differently inside local pressure maxima. Under the action of the strong differential advection imposed by the bump, a novel unstable mode develops and grows even when gas viscosity is large. Hence, pressure bumps are found to be the only places where streaming instability occurs in viscous discs. This offers a promising way to conciliate models of planet formation with recent observations of young discs.

Key words: planets and satellites: formation – protoplanetary discs.

1 INTRODUCTION

The main challenge of planet formation consists in figuring out how solids originating from the interstellar medium concentrate and grow over orders of magnitude up to form planetary cores (Chiang & Youdin 2010). Up to decimetric sizes, surface forces are strong enough for dust grains to grow by hit-and-stick collisions (Blum & Wurm 2008). This is not the case anymore for larger pebbles, and solid aggregates are expected instead to undergo bouncing or fragmentation (e.g. Güttler et al. 2010; Zsom et al. 2010). On the other hand, rocky structures should typically reach hundreds of metres in size to be glued by their own gravity. Thus, a third mechanism must bridge the gap and collect pebbles up the stage where their local weight becomes sufficient. Goodman & Pindor (2000) suggested that such a concentration may originate from a hydrodynamical instability. Youdin & Goodman (2005) and Youdin & Johansen (2007) demonstrated that the flow resulting from the radial drift of dust particles in weakly viscous discs is actually linearly unstable. In the non-linear regime, this so-called streaming instability develops dust overconcentrations (Johansen & Youdin 2007), which may ultimately form planetesimals by gravitational instabilities in discs of sufficient metallicities (Johansen et al. 2007; Johansen, Youdin & Mac Low 2009; Bai & Stone 2010c,b; Carrera, Johansen & Davies 2015). Hence, streaming instability may be responsible for the initial mass function of planetesimals in discs (Simon et al. 2016; Schäfer, Yang & Johansen 2017). The robustness of the streaming instability has been tested against several numerical schemes (Balsara et al. 2009; Bai & Stone 2010a; Miniati 2010; Tilley et al. 2010; Johansen, Youdin & Lithwick 2012; Johansen et al. 2014), towards the aim of simulating its effect in a global disc (Kowalik et al. 2013; Lyra & Kuchner 2013; Yang & Johansen 2014). Other physical processes such as vortices (Raettig, Klahr & Lyra 2015), photoevaporation (Carrera et al. 2017), presence of small grains (Laibe & Price 2014), grain growth (Drążkowska & Dullemond 2014) or snow lines (Schoonenberg & Ormel 2017) may reinforce the ability of streaming instability to concentrate dust.

Discs may therefore contain only a moderate amount of dust grains, since up to 50 per cent of their retained solid material may be converted into planetesimals (e.g. Johansen et al. 2015; Drążkowska, Alibert & Moore 2016). However, the emission from a continuous dense phase of millimetre grains is commonly detected in young discs (e.g. ALMA Partnership et al. 2015; Andrews et al. 2016), except at some specific locations. Dark rings are often associated with ongoing planet formation (e.g. Zhang, Blake & Bergin 2015; Gonzalez et al. 2015; Okuzumi et al. 2016) or even to planets (e.g. Dipierro et al. 2015; Dong, Zhu & Whitney 2015; Picogna & Kley 2015; Rosotti et al. 2016). To explain the persistence of the dust population almost everywhere, one may invoke the turbulent viscosity of the gas, which damps efficiently the small-scale perturbations at which streaming instability develops, but this would prevent planetesimal formation (see however Johansen et al. 2007; Dittrich, Klahr & Johansen 2013).

Such an interpretation is based on properties of the streaming instability derived for discs with monotonically decreasing pressure profiles. On the other hand, local pressure maxima may be created in the disc at some locations by internal processes (e.g. Béthune, Lesur & Ferreira 2016; Estrada, Cuzzi & Morgan 2016; Ruge et al. 2016; Gonzalez, Laibe & Maddison 2017). These pressure bumps are privileged locations for planetesimal formation since they concentrate dust (e.g. Nakagawa, Sekiya & Hayashi 1986; Haghighipour 2005). Finding a way for streaming instability to develop specifically in these pressure bumps would conciliate current

★ E-mail: guillaume.laibe@ens-lyon.fr

scenario of planetesimal formation and recent observations of discs. Simulations have been recently performed to show that streaming instability may deform the bump (Taki, Fujimoto & Ida 2016). So far, the resilience of the streaming instability against viscosity in pressure bumps has not been investigated.

In this study, we show that the development of the streaming instability in local pressure maxima is more complex than for discs with monotonic pressure profiles. We address the problem analytically by performing a linear perturbation analysis in a shearing box centred around a pressure maximum. In Section 2, we derive new solutions for the steady state, since pressure curvature provides additional advection compared to the usual case. The analysis of the unstable modes of the system as a function of the steepness of the bump is performed using a WKB approximation. The apparition of a second unstable mode for the streaming instability and its resilience against viscous damping are analysed in Section 3. Properties of this mode are brought back into the context of planet formation in Section 4.

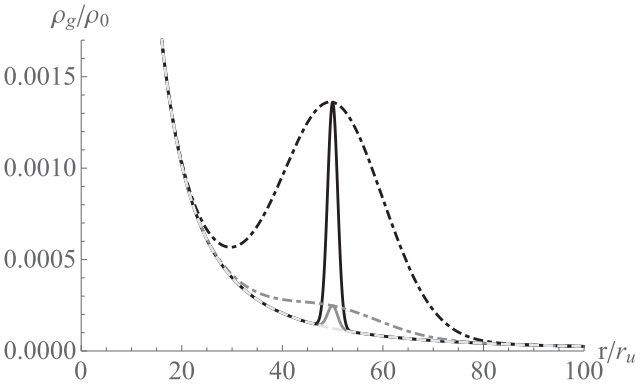

Figure 1. Zoomed-in density profiles around pressure bumps. Solid and dash–dotted lines correspond to relative width of the bump $\sigma/r_u = 1$ and $\sigma/r_u = 10$, while grey and black lines correspond to relative amplitudes $\tilde{A} = 1$ and $\tilde{A} = 10$, respectively. The gas density profile of exponents $p = 1$, $q = 0.4$ in absence of perturbation is given as a reference (dashed line/light grey).

2 EQUATIONS OF MOTION

2.1 Evolution in a global disc

2.1.1 Hypothesis

We consider non-self-gravitating, non-magnetic, vertically isothermal discs made of perfect gas. The background surface densities and temperatures of the gas are modelled by power laws of decreasing exponents, $\Sigma \propto r^{-p}$ and $T \propto r^{-q}$. We use $p = 1$ and $q = 0.4$ to be consistent with models which include detailed radiative transfer (e.g. Pinte & Laibe 2014). Under these assumptions, the gas density ρ_g and the pressure P in the midplane of the disc scale as $\rho_g \propto r^{-\xi}$ and $P \propto r^{-\xi-q}$, where $\xi \equiv p - q/2 + 3/2$. The effective viscosity of the disc is parametrized using an alpha prescription (Shakura & Sunyaev 1973). Numerical simulations of visco-turbulent discs exhibit values of $\alpha \sim 10^{-3}$–10^{-2} (e.g. Meheut et al. 2015). Dust grains are assumed to be compact, spherical, uncharged and of constant size and density. In observed discs (e.g. Williams & Best 2014), local gas surface densities are low enough for dust grains to be in the dilute Epstein drag regime (Epstein 1924; Baines, Williams & Asebiomo 1965). The drag stopping time of the particles is denoted $t_{\rm stop}$. For millimetre-in-size grains, $t_{\rm stop}$ is of the order of the orbital period at $\sim$50 au (Laibe, Gonzalez & Maddison 2012). The ratio between the drag and the orbital times, often called the Stokes number of the flow, is denoted τ_s, consistently with the notations of Youdin & Goodman (2005). The dust phase is modelled by a continuous viscousless and pressureless fluid (Saffman 1962; Garaud, Barrière-Fouchet & Lin 2004). The local dust-to-gas ratio $\epsilon \equiv \rho_p/\rho_g$ is larger than the typical 1 per cent of the interstellar medium since dust concentrates vertically and radially in the disc. We follow Youdin & Goodman (2005) and neglect the vertical stratification of the disc. Our study is therefore relevant for grains with typical sizes $\gtrsim$10μm which have settled close enough to the midplane (Dubrulle, Morfill & Sterzik 1995; Fromang & Nelson 2009).

2.1.2 Pressure maximum

We model a local pressure maximum by superimposing a Gaussian perturbation to the usual gas density profile, i.e.

$$\rho_g(r) = \rho_0 \left[\left(\frac{r}{r_u} \right)^{-\xi} + A e^{-\frac{(r-r_0)^2}{2\sigma^2}} \right]. \quad (1)$$

Hence, the amplitude and the width of the density maximum are parametrized by A and σ, respectively. The radial coordinate is scaled with a radius r_u and the Gaussian bump is centred around a position r_0. Fig. 1 shows different shapes of density profiles obtained when varying A and σ. Note that A should be large enough for the Gaussian perturbation to dominate locally over the decreasing background and thus, for the pressure maximum to exist. The relative amplitude $\tilde{A}$ of the maximum respectively to the background is

$$\tilde{A} \equiv A\,(r_0/r_u)^{\xi}. \quad (2)$$

$\tilde{A}$ varies from $\sim$0.1 for a perturbation due to a Neptune-like mass planet (e.g. Dipierro & Laibe 2017) up to $\sim$10 for self-induced dust traps (Gonzalez et al. 2017). The width of the bump σ is of the order of $\sim H$, the pressure scaleheight. In absence of any pressure maximum, or when the pressure perturbation is negligible, the orbital correction with respect to a pure Keplerian rotation is of the order $\mathcal{O}\left(H^2/r^2\right)$. In a pressure bump, the orbital correction is of the order $\mathcal{O}\left(\tilde{A}\,H^2/\sigma^2\right)$ and should remain small enough for the disc to be supported by rotation.

2.2 Shearing box approximation

For simplicity, the evolution of gas and dust is studied in a local frame corotating with the disc at a location $\hat{r}_0$ and a frequency Ω_0. In this shearing box, the coordinates are expanded to the linear order (Goldreich & Lynden-Bell 1965), and $x \equiv r - \hat{r}_0$, $y \equiv \hat{r}_0\,(\theta - \Omega_0 t)$ and z denote the radial, azimuthal and vertical directions, respectively. In the shearing box approximation, the large-scale contribution of the background pressure gradient comes under the form of a constant force (Youdin & Goodman 2005). In a box centred around a pressure bump, the large-scale background pressure gradient is a linear function of the distance from the pressure maximum. For convenience, we centre the box around $\hat{r}_0 = r_0$, the maximum of the Gaussian perturbation. Expanding the pressure gradient term to the second order in x provides

$$-\frac{\nabla P}{\rho_g} \simeq 2 r_0 \Omega_0^2 \left(\eta + \frac{\Gamma}{2 r_0} x \right) \mathbf{u}_x, \quad (3)$$

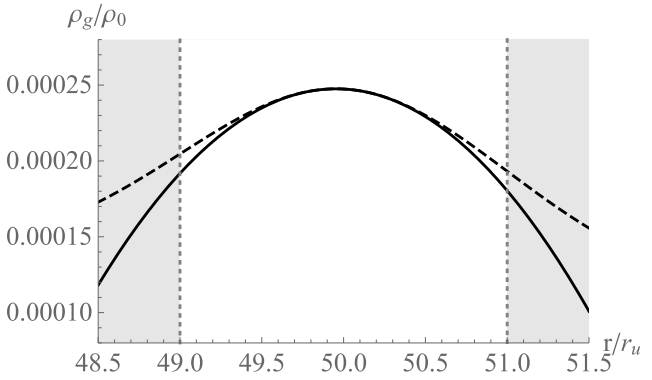

Figure 2. Acomparison between the gas density and its expansion used in the shearing box approximation (dashed and solid lines, respectively). Errors are of the order 1 per cent in L^1 norm, peaking at 5 per cent at the edges of the box of width $\pm\sigma$ delimited by a grey zone. The amplitude and width of the bump are $\tilde{A} = 1$ and $\sigma/r_u = 1$, respectively.

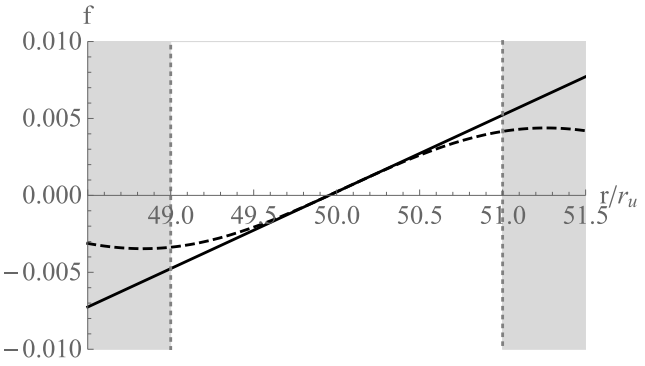

Figure 3. Similar to Fig. 2: comparison between the normalized pressure force (dashed line) and its linearization expansion (solid line) around r_0, the maximum of the Gaussian perturbation. Errors are of the order 10 per cent in L^1 norm, peaking at 20 per cent at the edges of the box.

with

$$\eta \equiv \frac{1}{2}\left.\frac{\mathrm{d}\ln\rho_g}{\mathrm{d}\ln r}\right|_{r_0}\left(\frac{H_0}{r_0}\right)^2, \tag{4}$$

$$\Gamma \equiv r_0^2\left.\frac{\mathrm{d}^2\ln\rho_g}{\mathrm{d}r^2}\right|_{r_0}\left(\frac{H_0}{r_0}\right)^2, \tag{5}$$

where H_0 denotes the scaleheight of the disc at r_0. Following Youdin & Goodman (2005) notations, we denote $\eta_0 = \eta|_{A=0}$ the pressure gradient term in absence of bump. Young protoplanetary discs are denser and warmer in the inner regions, which implies $\eta_0 > 0$. In typical discs, $\eta_0 \simeq 10^{-2}$. Note that discs with power-law profiles have in general non-zero values for Γ. This contribution from the curvature of the density profile is neglected in Youdin & Goodman (2005), which is an excellent approximation. A pressure bump is defined by $\Gamma > 0$. The pressure maximum position $x_{\max} \equiv -2r_0\eta/\Gamma$ is slightly shifted with respect to the centre of the box as a result of the small contribution of the decreasing unperturbed pressure profile. Using equation (1) in equations (4) and (5) gives

$$\eta \equiv \frac{\xi}{2(1+\tilde{A})}\left(\frac{H_0}{r_0}\right)^2, \tag{6}$$

$$\Gamma \equiv \left\{-\frac{\xi(\xi+1)}{1+\tilde{A}} + \frac{\xi^2}{(1+\tilde{A})^2}\right\}\left(\frac{H_0}{r_0}\right)^2 + \frac{\tilde{A}}{1+\tilde{A}}\left(\frac{H_0}{\sigma}\right)^2. \tag{7}$$

The first term of the right-hand side of equation (7) corresponds to the contribution of the background profile, which increases with ξ (steeper and more curved density profiles). The second term corresponds to the contribution added by the Gaussian perturbation and scales like $\tilde{A}\,(H_0/\sigma)^2$. The relative contribution between the maximum and the background is therefore of the order $\tilde{A}\,(r_0/\sigma)^2$. Fig. 2 shows that the size of the box is constrained by the validity of the linear approximation. For equation (3) to remain valid, the size of the box should not exceed $\sim\min(\sigma, H)$. Note that on the other hand, very narrow bumps may be Rayleigh unstable (Yang & Menou 2010). In practice, we use $\sigma = 1\,r_u$. The discrepancy between the real pressure force and its linear approximation is of the order ∼20 per cent at most at the edges of the box (Fig. 3). Viscous forces are similarly decomposed in large and small scales components. In a typical α −disc, the relative contribution between the viscosity and the radial pressure gradient is of the order $\alpha \ll 1$ at a large scale. This contribution is therefore neglected. On the other hand, the small-scale viscous forces, which damp local gas fluctuations, are treated as usual. To avoid unnecessary complications, the local gas sound speed c_s, the viscosity $\nu = \alpha c_s H$, the stopping time of dust grains $t_{\rm stop}$ and the background dust-to-gas ratio ϵ are assumed to be constant over the size of the box. This implies that there is more dust in the centre of the bump than at the edges. The equations of motion for the gas and the dust are therefore

$$\frac{\partial\rho_g}{\partial t} + \nabla\cdot(\rho_g\mathbf{V}_g) = 0, \tag{8}$$

$$\frac{\partial\rho_p}{\partial t} + \nabla\cdot(\rho_p\mathbf{V}_p) = 0, \tag{9}$$

$$\begin{aligned}\left(\frac{\partial}{\partial t} + \mathbf{V}_g\cdot\nabla\right)\mathbf{V}_g = &-r_0 x\left.\frac{\mathrm{d}\Omega_K^2}{\mathrm{d}r}\right|_{r_0}\mathbf{u}_x - 2\Omega_0\mathbf{u}_z\times\mathbf{V}_g\\ &+ 2r_0\Omega_0^2\left(\eta + \frac{\Gamma}{2r_0}x\right)\mathbf{u}_x + \nu\Delta\mathbf{V}_g\\ &+ \frac{\rho_p}{\rho_g}\frac{\mathbf{V}_p - \mathbf{V}_g}{t_{\rm stop}},\end{aligned} \tag{10}$$

$$\begin{aligned}\left(\frac{\partial}{\partial t} + \mathbf{V}_p\cdot\nabla\right)\mathbf{V}_p = &-r_0 x\left.\frac{\mathrm{d}\Omega_K^2}{\mathrm{d}r}\right|_{r_0}\mathbf{u}_x - 2\Omega_0\mathbf{u}_z\times\mathbf{V}_p\\ &- \frac{\mathbf{V}_p - \mathbf{V}_g}{t_{\rm stop}}.\end{aligned} \tag{11}$$

In particular, gas and dust have different advection velocities $\mathbf{V}_{g,p}$ and the drag from the dust on to the gas is not neglected (Youdin & Goodman 2005). For simplicity, physical quantities are used in a dimensionless form, i.e. $\tilde{\omega} \equiv \omega/\Omega_0$, $\tilde{x} \equiv x/\eta_0 r_0$, $\tilde{k} \equiv k\eta_0 r_0$ and $\tilde{v} \equiv v/\eta_0 r_0\Omega_0$. As a remark, equations (8)–(11) differ from the system studied by Taki et al. (2016), where the large-scale pressure gradient is similar to the constant background introduced in Youdin & Goodman (2005), and on top of which a small local Gaussian perturbation of width half of the box is superimposed. This situation corresponds to a pressure perturbation developing at small scales which is weak enough for not affecting background radial velocities of the gas and the dust.

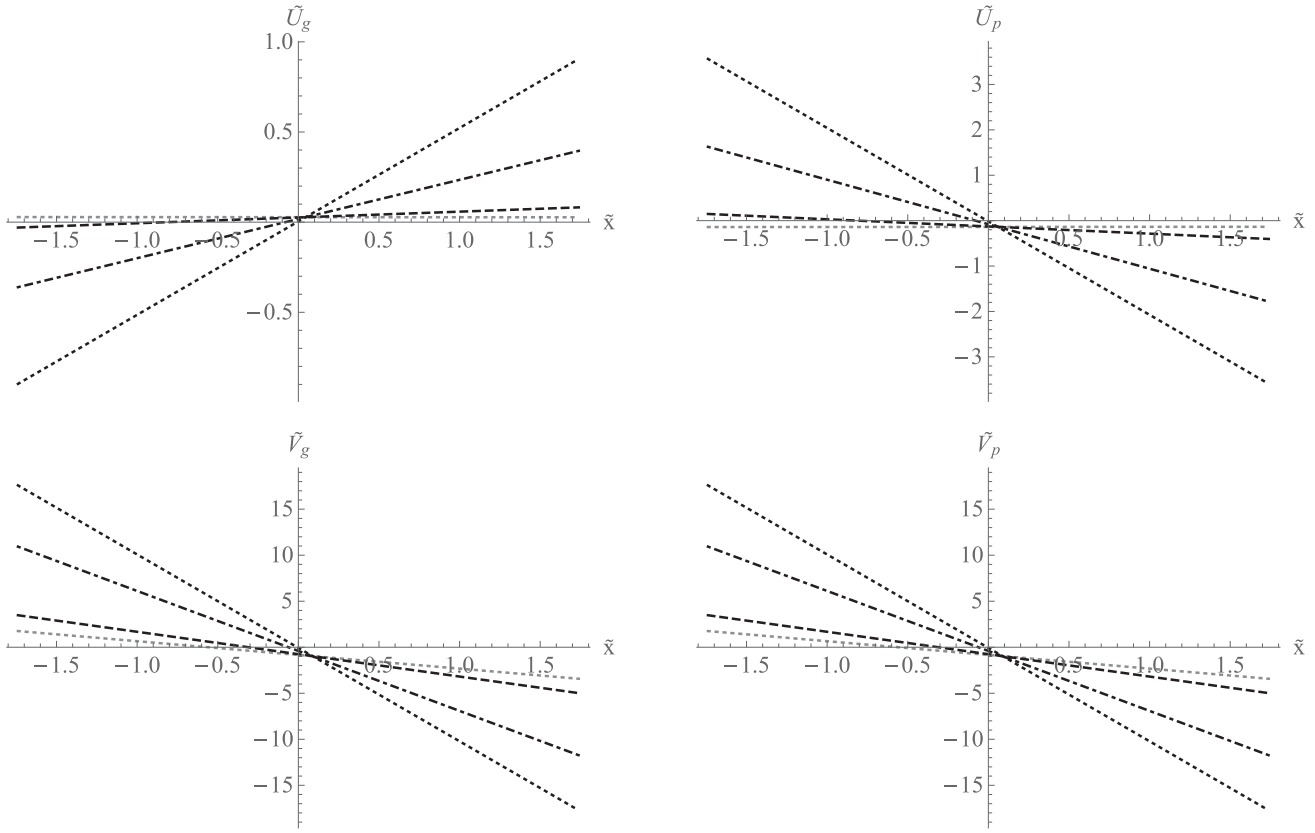

Figure 4. Radial and azimuthal (top/bottom) velocities for the gas and the dust (left/right) in the box. Bumps with relative amplitudes $\tilde{A} = 0.1-1-10$ are considered (dashed, dot–dashed and dotted black lines), other parameters being those of the `linB` problem. Velocities in absence of pressure bump are indicated for a reference (grey dotted lines).

2.3 Steady state

The steady-state velocities for gas and dust in the pressure maximum are determined by seeking for solutions of the form $(\overline{U}_g, \overline{V}_g) = (a_g x + b_g, \alpha_g x + \beta_g)$ and $(\overline{U}_p, \overline{V}_p) = (a_p x + b_p, \alpha_p x + \beta_p)$. The linear dependence of the velocities with respect to x is enforced to ensure consistency between the presence of the pressure maximum and the shearing box formalism. Using this Ansatz in equations (8)–(11) provides the *non-linear* system of equations

$$a_p^2 - 3\Omega_0^2 - 2\Omega_0\alpha_p + \frac{1}{t_{stop}}(a_p - a_g) = 0, \tag{12}$$

$$a_p b_p - 2\Omega_0\beta_p + \frac{1}{t_{stop}}(b_p - b_g) = 0, \tag{13}$$

$$a_p\alpha_p + 2\Omega_0 a_p + \frac{1}{t_{stop}}(\alpha_p - \alpha_g) = 0, \tag{14}$$

$$b_p\alpha_p + 2\Omega_0 b_p + \frac{1}{t_{stop}}(\beta_p - \beta_g) = 0, \tag{15}$$

$$a_g^2 - 3\Omega_0^2 - 2\Omega_0\alpha_g - \frac{\epsilon}{t_{stop}}(a_p - a_g) - \Gamma\Omega_0^2 = 0, \tag{16}$$

$$a_g b_g - 2\Omega_0\beta_g - \frac{\epsilon}{t_{stop}}(b_p - b_g) - 2r_0\Omega_0^2\eta = 0, \tag{17}$$

$$a_g\alpha_g + 2\Omega_0 a_g - \frac{\epsilon}{t_{stop}}(\alpha_p - \alpha_g) = 0, \tag{18}$$

$$b_g\alpha_g + 2\Omega_0 b_g - \frac{\epsilon}{t_{stop}}(\beta_p - \beta_g) = 0. \tag{19}$$

These non-linear terms originate from non-trivial advection terms specific to the pressure bump and require care for numerical root finding (see Appendix B for technical details). Neglecting this additional advection provides a crude approximation of the solution of equations (12)–(19) by taking the solution of Nakagawa et al. (1986) given in Appendix B and replacing η by $\eta + \frac{\Gamma}{2r_0}x$. We find errors of the order $\sim$10 per cent up to $\sim$100 per cent between the two approaches, a discrepancy becoming important for the radial velocity of the gas. Fig. 4 illustrates the dust and the gas motion inside the bump for various relative amplitudes of the pressure maximum. As a reminder, pure Keplerian shear is $v_y = -\frac{3}{2}\Omega_0 x$. In absence of a bump, dust (resp. gas) drifts inwards (resp. outwards) by conservation of angular momentum. Both the gas and the dust are sub-Keplerian. Inside a bump, dust drifts towards the pressure maximum, while gas drifts outwards. This requires for gas and dust to orbit at super-Keplerian frequency in the inner edge of the bump. Both the gas and the dust radial velocities are rigorously zero at $x_{max} < 0$ the location of the pressure maximum. Although the different velocities appear to cross each other at the same location in Fig. 4, this is actually not the case. Mathematically, the intersection between the line corresponding to $\tilde{A} = 0$ and the other lines depends slightly on the different physical parameters. In particular, for increasing values of Γ, the intersecting point becomes closer to the centre of the box.

2.4 Perturbation

The linear stability of the system equations (8)–(11) is investigated by looking for perturbations of the form

$$\rho_{\rm g} = \rho_{\rm g}^0(1+\delta_{\rm g}), \tag{20}$$

$$\rho_{\rm p} = \rho_{\rm p}^0(1+\delta_{\rm p}), \tag{21}$$

$$\mathbf{V}_{\rm g} = \overline{\mathbf{V}}_{\rm g} + \mathbf{v}_{\rm g} = \overline{\mathbf{V}}_{\rm g} + u_{\rm g}\mathbf{u}_x + v_{\rm g}\mathbf{u}_y + w_{\rm g}\mathbf{u}_z, \tag{22}$$

$$\mathbf{V}_{\rm p} = \overline{\mathbf{V}}_{\rm p} + \mathbf{v}_{\rm p} = \overline{\mathbf{V}}_{\rm p} + u_{\rm p}\mathbf{u}_x + v_{\rm p}\mathbf{u}_y + w_{\rm p}\mathbf{u}_z, \tag{23}$$

where

$$\delta(x,z,t) = \Delta(x)e^{i(k_x x + k_z z - \omega t)}. \tag{24}$$

In absence of a pressure bump, the perturbation must develop in both the x and the z direction to become unstable (Youdin & Goodman 2005; Jacquet, Balbus & Latter 2011). This property originates from local conservation of the gas mass. With a pressure bump, advection terms enforce the amplitude of the perturbation Δ to depend on x. For simplicity, we focus on cases where this amplitude varies slowly compared to the phase ($Hk_x \gg 1$) and use a WKB approximation to compute spatial derivatives, i.e.

$$\frac{\partial\delta(x,z,t)}{\partial x} \simeq ik_x\Delta(x)e^{i(k_x x + k_z z - \omega t)}. \tag{25}$$

We obtain the following set of eight linear equations for the perturbation

$$-i\omega\delta_{\rm g} + i\delta_{\rm g}k_x\overline{U}_{\rm g} + \delta_{\rm g}a_{\rm g} + ik_x u_{\rm g} + ik_z w_{\rm g} = 0, \tag{26}$$

$$-i\omega\delta_{\rm p} + i\delta_{\rm p}k_x\overline{U}_{\rm p} + \delta_{\rm p}a_{\rm p} + ik_x u_{\rm p} + ik_z w_{\rm p} = 0, \tag{27}$$

$$\begin{aligned}&-i\omega\mathbf{v}_{\rm g} + ik_x\overline{U}_{\rm g}\mathbf{v}_{\rm g} + (u_{\rm g}a_{\rm g} - 2v_{\rm g}\Omega_0)\mathbf{u}_x + u_{\rm g}(\alpha_{\rm g}+2\Omega_0)\mathbf{u}_y\\ &- \frac{\epsilon}{t_{\rm stop}}(\mathbf{v}_{\rm p} - \mathbf{v}_{\rm g} + (\delta_{\rm p}-\delta_{\rm g})(\overline{\mathbf{V}}_{\rm p} - \overline{\mathbf{V}}_{\rm g}))\\ &+ ic_s^2\delta_{\rm g}\mathbf{k} + \nu(k_x^2+k_z^2)\mathbf{v}_{\rm g} = 0,\end{aligned} \tag{28}$$

$$\begin{aligned}&-i\omega\mathbf{v}_{\rm p} + ik_x\overline{U}_{\rm p}\mathbf{v}_{\rm p} + (u_{\rm p}a_{\rm p} - 2v_{\rm p}\Omega_0)\mathbf{u}_x + u_{\rm p}(\alpha_{\rm p}+2\Omega_0)\mathbf{u}_y\\ &+ \frac{1}{t_{\rm stop}}(\mathbf{v}_{\rm p} - \mathbf{v}_{\rm g}) = 0,\end{aligned} \tag{29}$$

where the four background velocities $\overline{U}_{\rm g}$, $\overline{U}_{\rm p}$, $\overline{V}_{\rm g}$ and $\overline{V}_{\rm p}$ are the linear functions determined in Section 2.3 and not the solutions derived by Nakagawa et al. (1986). In practice, the eigenmodes $\omega_{1,8}$ of the system equations (26)–(29) are determined by finding zeros of the determinant of the perturbation matrix numerically, using a sufficient precision. Note that the eigenmodes obtained by this procedure depend on x, i.e. $\omega_{1,8}(x)$, which may sound inconsistent with equation (24). However, at small times,

$$k_x^{-1}\frac{{\rm d}\omega}{{\rm d}x}t \simeq \frac{\Omega_0 t}{k_x H}. \tag{30}$$

In this case, the solution is consistent with the initial Ansatz and the WKB approximation over a number $n = k_x H \gg 1$ of orbital periods. To compare our results with the case of an inviscid disc with no pressure bump, we use the test cases `linA, linB, linC and linD` studied in Youdin & Johansen (2007) and Bai & Stone (2010a) (see parameters in Appendix A). Our procedure provides the expected coefficients with similar precision.

3 RESULTS

3.1 Unstable modes

The growth rates s obtained from the procedure described in Section 2.4 are shown in Fig. 5. Three modes are considered: two modified epicyclic modes and the secular mode of the streaming instability identified in Youdin & Goodman (2005), the other modes playing no particular role in this problem. For tiny perturbations of the pressure profile, the only unstable mode is the secular mode, similarly to what happens in a disc with no bump. Novel features appear when increasing progressively the relative amplitude of the bump. Fig. 5 shows that one of the two epicyclic modes becomes unstable. The related growth rate may become larger than the growth rate of the secular mode as the amplitude of the bump increases. The possible instability of the epicyclic modes was mentioned in Youdin & Goodman (2005). When increasing further the amplitude of the bump, a transition between two distinct regimes occurs for relative amplitudes of the order $\tilde{A} \gtrsim 0.2$, a conservative value for typical bumps. Fig. 5 shows that a bifurcation between the secular and the stable epicyclic modes gives birth to two new modes. We find that this bifurcation is universal and, in particular, does not depend on the dust-to-gas ratio. The exact number of unstable modes depends on the distance to the pressure maximum. Near $x_{\rm max}$, two modes are unstable, whereas at the edges of the bump, only one mode is unstable. This mode corresponds to the novel unstable mode originating from the bifurcation and is not the secular mode of the streaming instability which grows in absence of maximum.

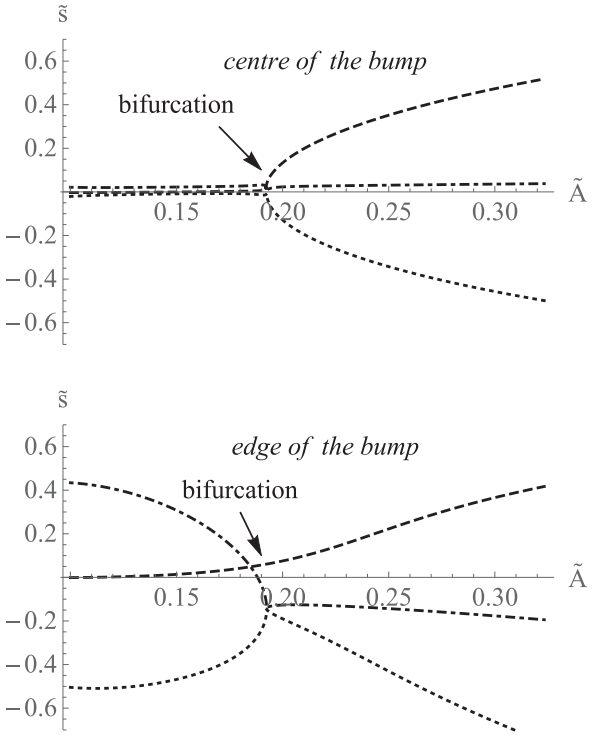

Figure 5. Growth rates of the two epicyclic modes and the secular mode of the streaming instability for increasing values of the relative amplitude $\tilde{A}$ of the bump. In absence of any pressure maximum, the only unstable mode is the usual secular mode (dot–dashed/black). In pressure maxima, a novel unstable mode develops (dashed/black). A bifurcation between the secular mode and the other epicycle (dotted/black) occurs at $\tilde{A} \simeq 0.2$. Parameters correspond to the `linA` problem.

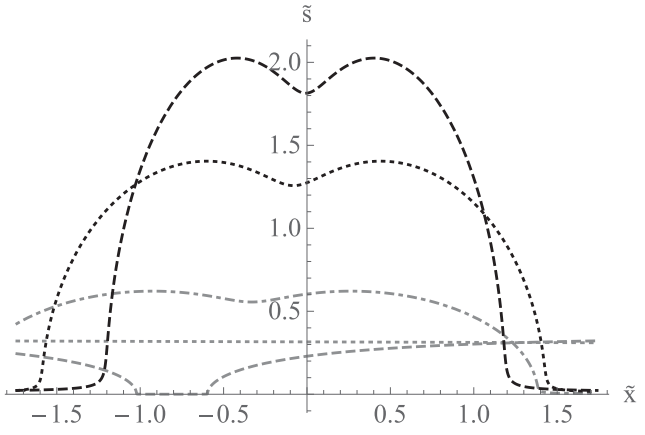

Figure 6. Growth rate of the streaming instability in the box for bumps of relative amplitudes $\tilde{A} = 0.1-0.25-1-10$ (dashed/grey, dot–dashed/grey, dotted/black and dashed/black, respectively). For shallow bumps, streaming instability develops everywhere except near the maximum where the pressure gradient is zero. For large bumps, the instability develops more efficiently close to the maximum. Parameters are those of the `linD` problem. The growth rate in absence of maximum is given by the dotted/grey line.

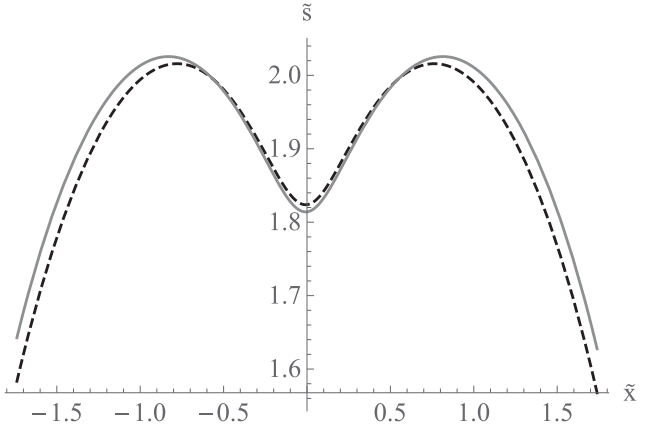

Figure 7. Growth rate of the instability for two same ratios $\lambda/l_{\rm stop} = 1$. Growth rates are almost similar, discrepancies of a few per cent originating from slightly different advection velocities. We use $\tilde{A} = 10, \epsilon = 2, \tau_{\rm s} = 0.01$, $\tilde{k}_{x,z} = 100$ (black dashed line) and $\tau_{\rm s} = 0.001, \tilde{k}_{x,z} = 1000$ (grey solid line).

Physically, this novel instability originates from the strong differential advection between the gas and the dust at the edges of the bump powered by the background velocities in the bump.

Fig. 6 shows how the growth rates depend on the radial location in the bump for increasing amplitudes, showing the consequences of the bifurcation identified above. Rigorously, the exact location of the pressure maximum depends on $\tilde{A}$ and is slightly offset from the centre of the shearing box due to the local curvature of the pressure profile in absence of maximum (see Section 2.3). For shallow bumps ($\tilde{A} \lesssim 0.2$), streaming instability develops everywhere except close to the pressure maximum. Its efficiency is maximum at the edges of the bump, where the local pressure gradient is the greatest. This behaviour is consistent with the linear analysis of Youdin & Goodman (2005), valid for discs with monotonic pressure profiles. For larger amplitudes ($\tilde{A} \gtrsim 0.2$), the streaming instability grows more efficiently in the centre of the bump than at the edges. As

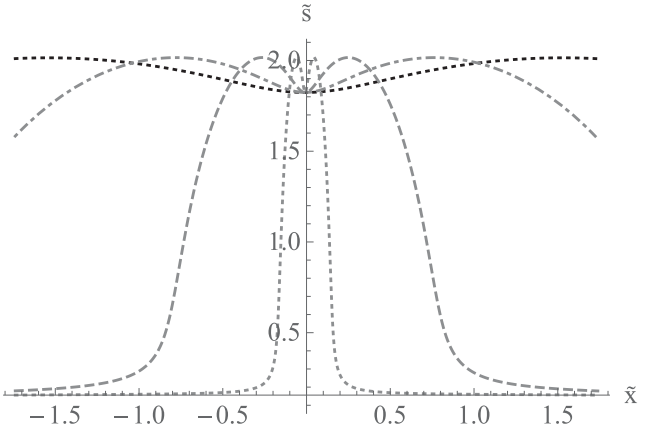

Figure 8. Growth rates for a bump of relative amplitude $\tilde{A} = 10$ and different wavenumbers $\tilde{k}_{x,z} = 50-100-300-1500$ (dotted/black, dot–dashed/grey, dashed/grey, dotted/grey). The region where the instability develops is more extended for larger wavelengths. Parameters are those of the `linC` problem.

shown in Fig. 6, its efficiency is slightly reduced at $x = x_{\rm max}$. At the edges of the bump, the growth rate decreases up to eventually reach zero. No instability develops in this particular case. Hence, for a shallow bump in an inviscid disc, gas and dust are linearly unstable everywhere except at the exact location of the pressure maximum. On the opposite, when the disc contains a bump which is large enough (i.e. for pressure perturbation to be of a least a few ten per cents), dust concentration may occur preferentially inside the maximum, and not at the edges, as one would have expected with the classical linear stability analysis.

The growth rates depend on the ratio between the wavelength λ of the perturbation and $l_{\rm stop} \equiv \eta_0 r_0 \Omega_0 t_{\rm stop}$, the length over which the gas decouples from the dust, sometimes referred as the stopping length. The ratio $\lambda/l_{\rm stop}$ measures the number of perturbations over which the stopping length spreads. Fig. 7 shows that for similar values of $\lambda/l_{\rm stop}$ or equivalently $\tilde{k}_{x,z}\,\tau_{\rm s}$, the growth rates obtained are almost identical. Corrections of the order a few per cent are due to slightly different values for the advection velocities. Fig. 8 shows growth rates obtained for different wavelengths λ. For $l_{\rm stop} \gg \lambda$, dust and gas experience the details of the pressure profile before being coupled together by the drag, and the growth rate profile is narrow. Instead, for $l_{\rm stop} < \lambda$, dust and gas are quickly coupled by the drag, their differential velocity is proportional to the local pressure gradient, and this information is carried away by the perturbation. In this case, the growth rate profile is wider. The ratio $\lambda/l_{\rm stop}$ sets the width of the region where no instability develops for shallow bumps, and the width of the central region where the instability is weakened for large bumps.

3.2 Viscosity

The ability for viscosity to damp the instability is now investigated. Fig. 9 shows that in absence of a pressure bump, viscosity prevents the development of the streaming instability for values of α as low as $\sim 10^{-5}$. This value depends on the wavelength of the perturbation, smaller fluctuations being damped more efficiently by viscosity. Streaming instability therefore does not grow in typical visco-turbulent discs where $\alpha \sim 10^{-3}$–10^{-2}. However, when a significant bump is present in the disc, a different behaviour is

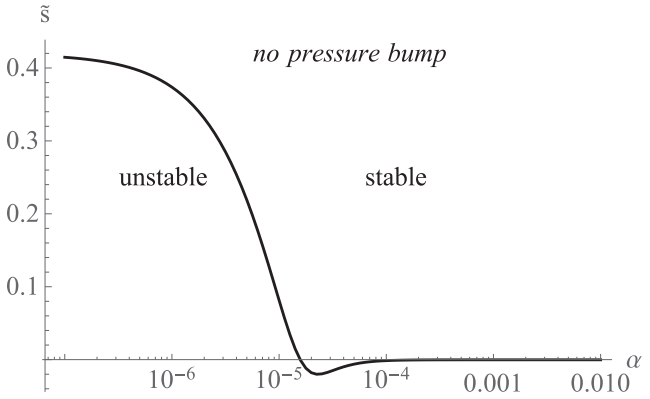

Figure 9. Growth rate of the instability in absence of bump for increasing viscosities. The unstable mode is damped for $\alpha \gtrsim 10^{-5}$. Parameters correspond to the `linA` problem.

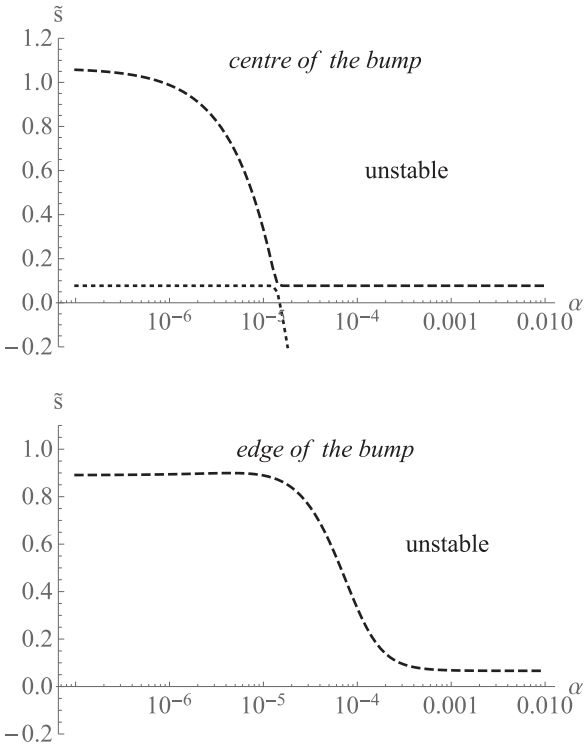

Figure 10. Growth rates of the unstable modes for increasing viscosities. An unstable mode exists even in highly viscous discs. Its growth rate is weakened by one order of magnitude compared to the inviscid case. Parameters correspond to the `linA` problem.

observed. Fig. 10 shows that for increasing values of α, one of the two unstable modes is suppressed, whereas the other one is only weakened, but not damped. The growth rate is reduced by one order of magnitude compared to the inviscid case (see Fig. 11). Still, this mode develops in a time relevant for planetesimal formation (see Section 4). Hence, streaming instability is found to always develop in a pressure bump, even in highly viscous discs. The fact that viscosity does not entirely damp the instability in the bump may appear counterintuitive. This apparent conundrum can be explained by noting that viscosity damps only the perturbations of the gas velocity.

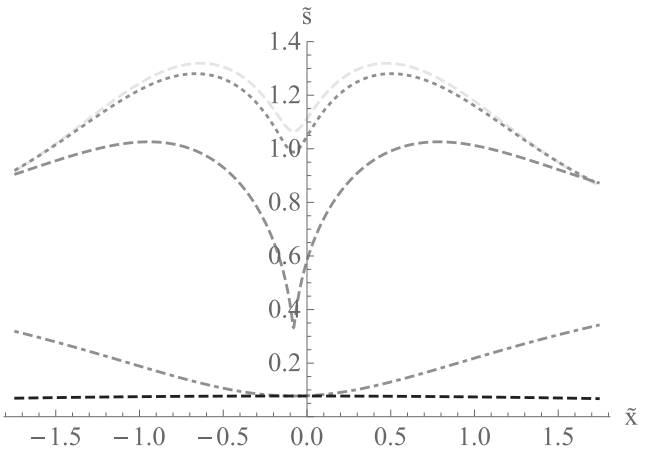

Figure 11. Growth rates for viscous parameters $\alpha = 0$–10^{-6}–10^{-5}–10^{-4}–10^{-3} (dashed/light, dotted, dashed, dash–dotted grey and dashed/black lines, respectively). Parameters are those of the `linA` problem, the relative amplitude of the bump is $\tilde{A} = 1$.

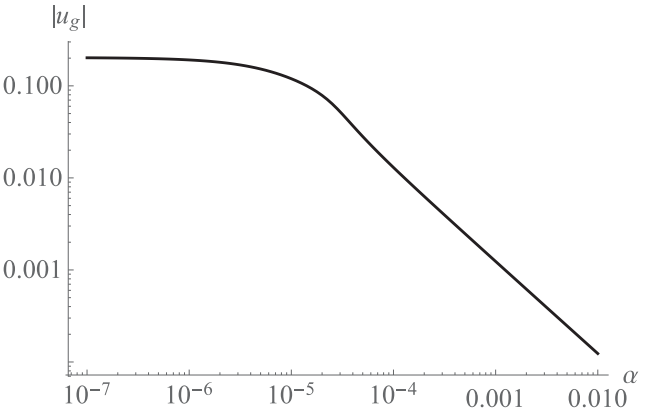

Figure 12. Amplitude of the perturbation of the radial velocity of the gas $|u_g|$ for increasing viscosities. The fluctuations are damped efficiently at large viscosities. The instability does not require fluctuations in the gas velocity to grow, since differential back-reaction is provided by the bump itself. Parameters are those of the `linA` problem.

Fig. 12 shows that these perturbations are actually suppressed more and more efficiently when viscosity increases. However, in pressure bumps, the required gradients of back-reaction are provided by the background velocities resulting from the local pressure profile. Hence, the instability can grow even if perturbations in the gas velocity are damped by viscosity. This effect is not observed in a disc with monotonic pressure profiles, since local gradients of back-reaction originate only from perturbations of the gas velocity which are killed by viscosity. Consistently, growth rates in the viscous regime do almost not depend on the wavelength, as shown in Fig. 13. Figs 14 and 15 show that similarly to the usual case, streaming instability is most efficient for $\tau_s \sim 1$ and $\epsilon \sim 1$, such parameters being typical protoplanetary discs.

Fig. 16 summarizes where streaming instability develops in discs, whether a pressure bump is present or not and whether the disc is inviscid or viscous. A dusty disc with monotonic pressure profile is linearly unstable everywhere if it is inviscid, and stable everywhere if it is viscous (Youdin & Goodman 2005). The

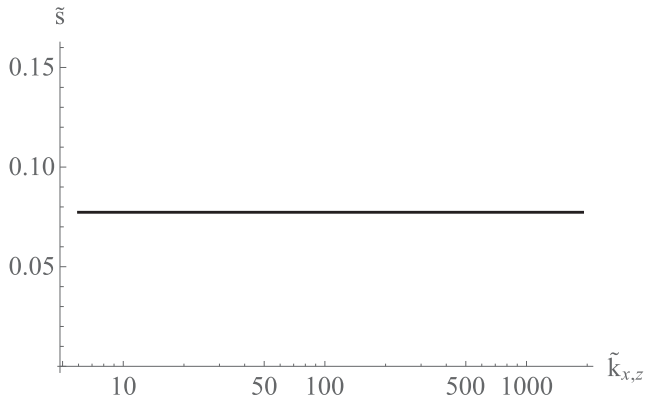

Figure 13. Growth rate of the instability for different wavenumbers $\tilde{k}_{x,z}$ in a viscous disc with $\alpha = 10^{-2}$. No dependence is found, consistently with a mechanism powered by the background profile of the bump. Parameters are those of the `linA` problem.

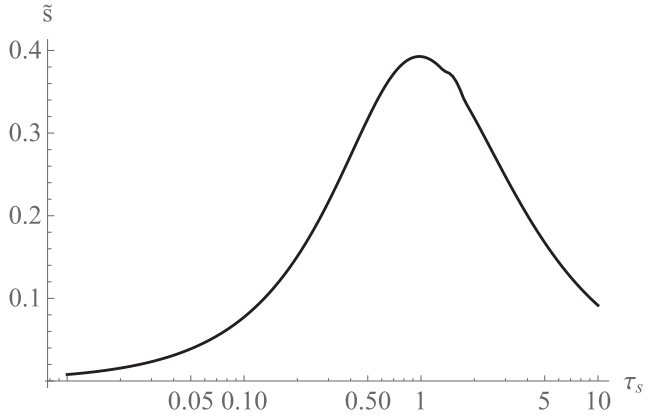

Figure 14. Growth rate of the instability as a function of the Stokes number τ_s for $\alpha = 10^{-2}$. Maximal efficiency is reached for $\tau_s \sim 1$ as expected. Parameters are those of the `linA` problem.

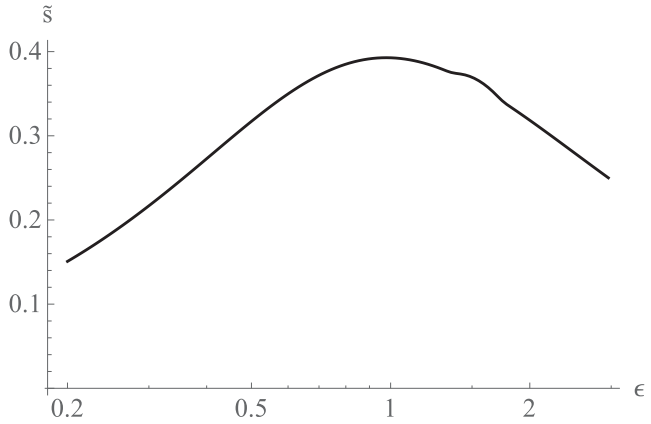

Figure 15. Growth rate of the instability as a function of the dust-to-gas ratio ϵ for $\alpha = 10^{-2}$. Maximal efficiency is reached for $\epsilon \sim 1$ as expected. Parameters are those of the `linA` problem.

latter is not true anymore in presence of a pressure maximum: streaming instability always grows in the bump, even if the disc is viscous.

4 DISCUSSION

We now verify that the assumptions made in Section 3 are consistent with the global evolution of the disc. The dust-to-gas ratio, the stopping time and the background velocities have been assumed to be constant during the time $t_{\rm growth}$ it takes for the instability to grow. Fig. 17 compares $t_{\rm growth}$ to the drift time of dust into the bump $t_{\rm drift}$ and shows that in the inviscid case, the disc remains in a steady state during the growth of the perturbation since $t_{\rm growth} \ll t_{\rm drift}$. In viscous discs, $t_{\rm growth}$ increases by one order of magnitude and the two time-scales become comparable. Long-lived global numerical simulations are therefore required to determine how the instability develops in this case. Moreover, the local depletion of gas caused by back-reaction empties the bump. Its lifetime is compared to the growing time by estimating the ratio $t_{\rm drift}/t_{\rm growth}\epsilon$. As long as $\epsilon \sim 1$, this condition is similar to the precedent one. Hence, our assumptions are essentially valid in real discs and streaming instability is expected to develop linearly as described in Section 3.

Gonzalez et al. (2017) found that formation of pressure bumps can be triggered by the sole action of dust drag on to the gas, with a spatial resolution insufficient to capture streaming instability. Their fig. 9 shows that the relative amplitude of the bump is at least of the order a few ten per cent, even for viscous discs with $\alpha = 10^{-2}$. Streaming instability in self-induced dust traps offers therefore a promising way to build planetesimals at specific locations. Millimetre grains are converted efficiently into planetesimals – and potentially later on into planets – in the trap and only there. Such a scenario is consistent with the dark rings probed recently by ALMA. Similarly, streaming instability may also grow specifically at the edges of the gap created by a massive planet. Since the tidal torque from the planet acts both on dust and gas, it does not induce additional differential velocities and we expect the results derived above to hold. Johansen et al. (2009) found that for large enough metallicities ($Z \gtrsim 0.03$), dust clumps formed by streaming instability collapse gravitationally. We expect a similar trend in a pressure bump, although numerical simulations at high resolution are required to investigate the non-linear stages of the instability.

5 CONCLUSION

In this study, we extend the linear theory of streaming instability in dusty protoplanetary discs to include the eventual presence of local pressure maxima, where solids drift in and pile up. We find that for pressure bumps with a relative amplitude larger than ∼20 per cent, a bifurcation occurs, giving birth to a novel unstable mode. The instability is powered by the strong differential advection locally imposed by the bump and as such, is resilient against viscous damping from the gas. The growth rate of the instability is typically reduced by one order of magnitude compared to the inviscid case. Hence, in viscous discs, streaming instability is found to grow in and only in local pressure maxima. In particular, streaming instability in self-induced dust traps provides a scenario for the early stages of planet formation consistent with the recent millimetre observations of dark rings in young discs. Numerical simulations are required to investigate the further non-linear development of the instability.

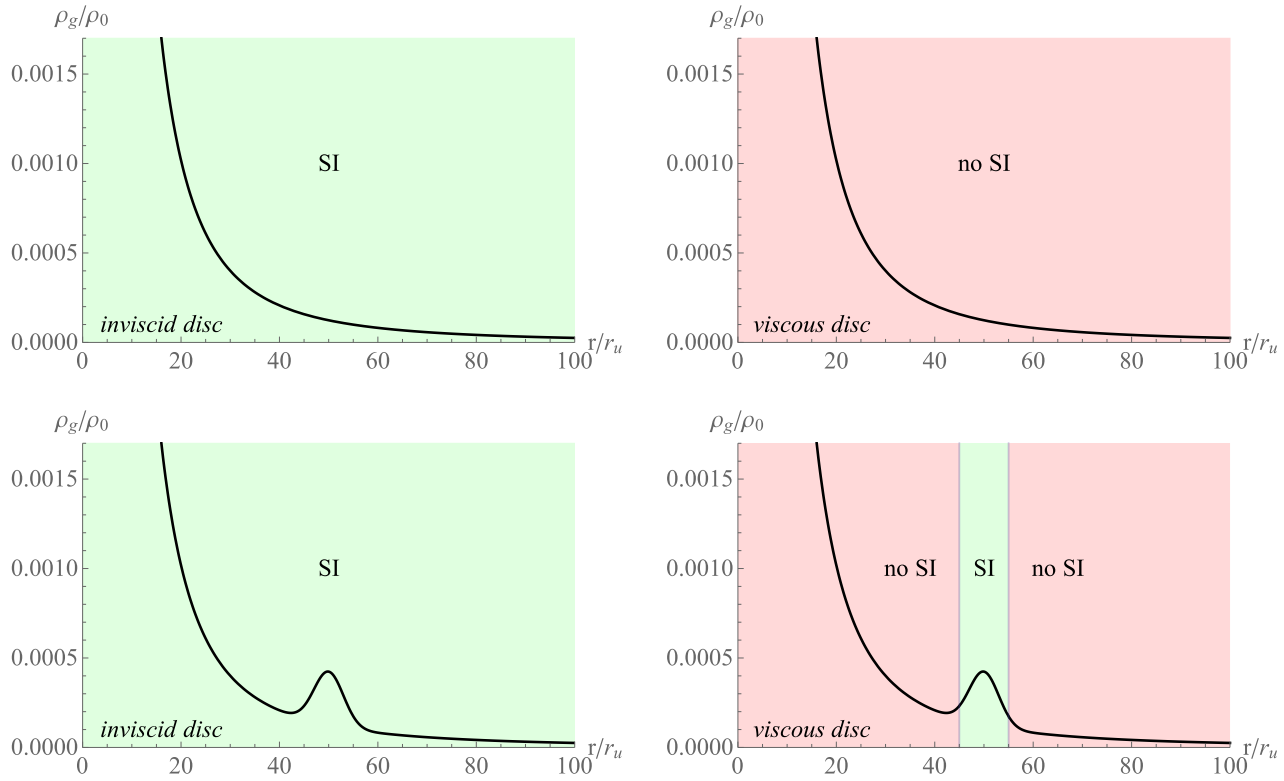

Figure 16. Sketch illustrating where the streaming instability grows in different discs. An inviscid disc is linearly unstable everywhere, with or without a pressure bump. In visco-turbulent discs, the streaming instability develops only inside pressure bumps.

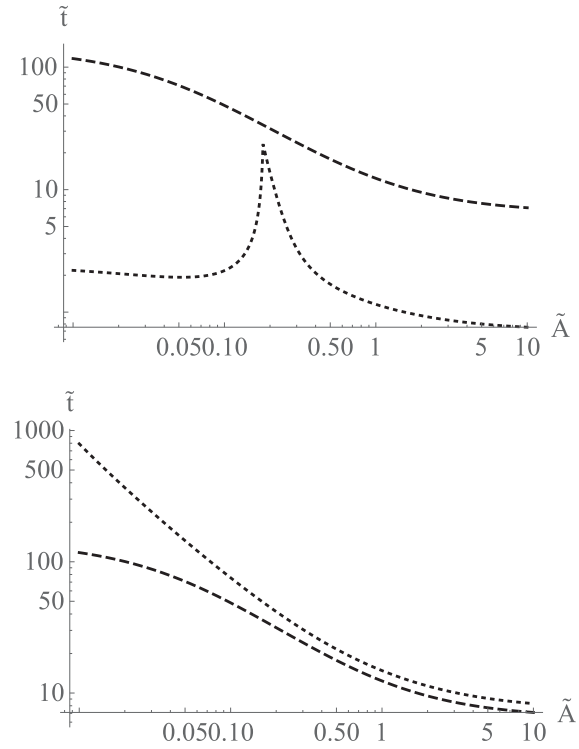

Figure 17. Time-scales of streaming instability (dotted/black) and dust drift (dashed/black) at the outer edge of the pressure bump. Top: inviscid disc, instability grows faster than dust drifts. Bottom: viscous disc ($\alpha = 10^{-3}$), the two time-scales are comparable for significant pressure bumps. Parameters correspond to the `linA` problem.

ACKNOWLEDGEMENTS

We acknowledge financial support from PNP, PNPS, PCMI of CNRS/INSU, CEA and CNES, France.

REFERENCES

ALMA Partnership et al., 2015, ApJ, 808, L3
Andrews S. M. et al., 2016, ApJ, 820, L40
Bai X.-N., Stone J. M., 2010a, ApJS, 190, 297
Bai X.-N., Stone J. M., 2010b, ApJ, 722, L220
Bai X.-N., Stone J. M., 2010c, ApJ, 722, 1437
Baines M. J., Williams I. P., Asebiomo A. S., 1965, MNRAS, 130, 63
Balsara D. S., Tilley D. A., Rettig T., Brittain S. D., 2009, MNRAS, 397, 24
Béthune W., Lesur G., Ferreira J., 2016, A&A, 589, A87
Blum J., Wurm G., 2008, ARA&A, 46, 21
Carrera D., Johansen A., Davies M. B., 2015, A&A, 579, A43
Carrera D., Gorti U., Johansen A., Davies M. B., 2017, ApJ, 839, 16
Chiang E., Youdin A. N., 2010, Annu. Rev. Earth Planet. Sci., 38, 493
Dipierro G., Laibe G., 2017, MNRAS, 469, 1932
Dipierro G., Price D., Laibe G., Hirsh K., Cerioli A., Lodato G., 2015, MNRAS, 453, L73
Dittrich K., Klahr H., Johansen A., 2013, ApJ, 763, 117
Dong R., Zhu Z., Whitney B., 2015, ApJ, 809, 93
Drążkowska J., Dullemond C. P., 2014, A&A, 572, A78
Drążkowska J., Alibert Y., Moore B., 2016, A&A, 594, A105
Dubrulle B., Morfill G., Sterzik M., 1995, Icarus, 114, 237
Epstein P. S., 1924, Phys. Rev., 23, 710
Estrada P. R., Cuzzi J. N., Morgan D. A., 2016, ApJ, 818, 200
Fromang S., Nelson R. P., 2009, A&A, 496, 597
Garaud P., Barrière-Fouchet L., Lin D. N. C., 2004, ApJ, 603, 292
Goldreich P., Lynden-Bell D., 1965, MNRAS, 130, 125
Gonzalez J.-F., Laibe G., Maddison S. T., Pinte C., Ménard F., 2015, MNRAS, 454, L36

Gonzalez J.-F., Laibe G., Maddison S. T., 2017, MNRAS, 467, 1984
Goodman J., Pindor B., 2000, Icarus, 148, 537
Güttler C., Blum J., Zsom A., Ormel C. W., Dullemond C. P., 2010, A&A, 513, A56
Haghighipour N., 2005, MNRAS, 362, 1015
Jacquet E., Balbus S., Latter H., 2011, MNRAS, 415, 3591
Johansen A., Youdin A., 2007, ApJ, 662, 627
Johansen A., Oishi J. S., Low M., Klahr H., Henning T., Youdin A., 2007, Nature, 448, 1022
Johansen A., Youdin A., Mac Low M.-M., 2009, ApJ, 704, L75
Johansen A., Youdin A. N., Lithwick Y., 2012, A&A, 537, A125
Johansen A., Blum J., Tanaka H., Ormel C., Bizzarro M., Rickman H., 2014, in Beuther H., Klessen R. S., Dullemond C. P., Henning T., eds, Protostars and Planets VI. Univ. of Arizona, Tucson. p. 547
Johansen A., Mac Low M.-M., Lacerda P., Bizzarro M., 2015, Sci. Adv., 1, 1500109
Kowalik K., Hanasz M., Wóltański D., Gawryszczak A., 2013, MNRAS, 434, 1460
Laibe G., Price D. J., 2014, MNRAS, 444, 1940
Laibe G., Gonzalez J.-F., Maddison S. T., 2012, A&A, 537, A61
Lyra W., Kuchner M., 2013, Nature, 499, 184
Meheut H., Fromang S., Lesur G., Joos M., Longaretti P.-Y., 2015, A&A, 579, A117
Miniati F., 2010, J. Comput. Phys., 229, 3916
Nakagawa Y., Sekiya M., Hayashi C., 1986, Icarus, 67, 375
Okuzumi S., Momose M., Sirono S.-i., Kobayashi H., Tanaka H., 2016, ApJ, 821, 82
Picogna G., Kley W., 2015, A&A, 584, A110
Pinte C., Laibe G., 2014, A&A, 565, A129
Raettig N., Klahr H., Lyra W., 2015, ApJ, 804, 35
Rosotti G. P., Juhasz A., Booth R. A., Clarke C. J., 2016, MNRAS, 459, 2790
Ruge J. P., Flock M., Wolf S., Dzyurkevich N., Fromang S., Henning T., Klahr H., Meheut H., 2016, A&A, 590, A17
Saffman P. G., 1962, J. Fluid Mech., 13, 120
Schäfer U., Yang C.-C., Johansen A., 2017, A&A, 597, A69
Schoonenberg D., Ormel C. W., 2017, A&A, 602, A21
Shakura N. I., Sunyaev R. A., 1973, A&A, 24, 337
Simon J. B., Armitage P. J., Li R., Youdin A. N., 2016, ApJ, 822, 55
Taki T., Fujimoto M., Ida S., 2016, A&A, 591, A86
Tilley D. A., Balsara D. S., Brittain S. D., Rettig T., 2010, MNRAS, 403, 211
Williams J. P., Best W. M. J., 2014, ApJ, 788, 59
Yang C.-C., Johansen A., 2014, ApJ, 792, 86
Yang C.-C., Menou K., 2010, MNRAS, 402, 2436
Youdin A. N., Goodman J., 2005, ApJ, 620, 459
Youdin A., Johansen A., 2007, ApJ, 662, 613
Zhang K., Blake G. A., Bergin E. A., 2015, ApJ, 806, L7
Zsom A., Ormel C. W., Güttler C., Blum J., Dullemond C. P., 2010, A&A, 513, A57

APPENDIX A: PARAMETERS OF THE LINEAR TESTS

The sets of parameters for the `linA`, `linB`, `linC` and `linD` problems are provided in Table A1.

Table A1. Parameters of the `linA`, `linB`, `linC` and `linD` problems, where $\eta_0 r_0 \Omega_0 / c_s = 0.05$.

Problem	$\tilde{k}_x$	$\tilde{k}_z$	τ_s	ϵ	$\tilde{s}$
`linA`	30	30	0.1	3	0.419 0204
`linB`	6	6	0.1	0.2	0.015 4764
`linC`	1500	1500	0.01	2	0.598 0690
`linD`	2000	2000	0.001	2	0.315 4373

APPENDIX B: SOLVING FOR BACKGROUND VELOCITIES

Solving equations (12)–(19) by elimination leads to a 256th-order polynomial equation in one of the variables (e.g. a_g), making the numerical resolution difficult. Simplifications can be made up to almost obtain an analytical solution. Combining equation (12) ± equation (16), equation (13) ± equation (17), equation (14) ± equation (18), equation (15) ± equation (19), we obtain

$$a^+a^- - 2\Omega_0\alpha^- + \gamma^+a^- + \Gamma\Omega_0^2 = 0, \tag{B1}$$

$$\frac{1}{2}a^+b^- + \frac{1}{2}a^-b^+ - 2\Omega_0\beta^- + \gamma^+b^- + 2r_0\eta\Omega_0^2 = 0, \tag{B2}$$

$$\frac{1}{2}a^+\alpha^- + \frac{1}{2}a^-\alpha^+ + 2\Omega_0a^- + \gamma^+\alpha^- = 0, \tag{B3}$$

$$\frac{1}{2}b^+\alpha^- + \frac{1}{2}b^-\alpha^+ + 2\Omega_0b^- + \gamma^+\beta^- = 0, \tag{B4}$$

$$\frac{1}{2}(a^+)^2 + \frac{1}{2}(a^-)^2 - 6\Omega_0^2 - 2\Omega_0\alpha^+ + \gamma^-a^- - \Gamma\Omega_0^2 = 0, \tag{B5}$$

$$\frac{1}{2}a^+b^+ + \frac{1}{2}a^-b^- - 2\Omega_0\beta^+ + \gamma^-b^- - 2r_0\eta\Omega_0^2 = 0, \tag{B6}$$

$$\frac{1}{2}a^+\alpha^+ + \frac{1}{2}a^-\alpha^- + 2\Omega_0a^+ + \gamma^-\alpha^- = 0, \tag{B7}$$

$$\frac{1}{2}b^+\alpha^+ + \frac{1}{2}b^-\alpha^- + 2\Omega_0b^+ + \gamma^-\beta^- = 0, \tag{B8}$$

where

$$\begin{aligned} a^\pm &\equiv a_p \pm a_g, \quad & b^\pm &\equiv b_p \pm b_g, \\ \alpha^\pm &\equiv \alpha_p \pm \alpha_g, \quad & \beta^\pm &\equiv \beta_p \pm \beta_g, \end{aligned} \tag{B9}$$

and $\gamma^\pm \equiv \frac{1\pm\epsilon}{t_{stop}}$. Equations (B1), (B3), (B5) and (B7) contain only $a^\pm$ and $\alpha^\pm$ and can be combined to obtain a^+ as a root of a much simpler fifth-order polynomial. No analytic root exists for such a polynomial. However, its single real root can easily be found numerically. From there, the determination of all the other quantities is algebraic, except choosing one root between the two of a second-order polynomial. Yet, one of the root is unphysical and can be easily discarded when looking at the numerical values (e.g. $V_p \simeq 10^3 r_0\Omega_0$). In the case $\eta = 0$ (pure maximum), we obtain analytically $b_{g,p} = \beta_{g,p} = 0$, i.e. the stationary velocities are centred around $x = 0$, as expected. The non-linearity of the system comes from non-linear advection terms, even in the steady state. Although alternative functional forms may solve the equations of motion, we restrain ourselves to a linear form to remain consistent with the shearing box approximation. In absence of any pressure maximum ($\Gamma = 0$), we obtain the expressions given in Youdin & Johansen (2007)

$$\overline{U}_g = \frac{2\epsilon\tau_s\eta r_0\Omega_0}{\tau_s^2 + (1+\epsilon)^2}, \tag{B10}$$

$$\overline{V}_g = -\frac{3}{2}\Omega_0 x - \eta r_0\Omega_0 + \frac{\epsilon(1+\epsilon)\eta r_0\Omega_0}{\tau_s^2 + (1+\epsilon^2)}, \tag{B11}$$

$$\overline{U}_p = \frac{-2\eta\tau_s r_0\Omega_0}{\tau_s^2 + (1+\epsilon)^2}, \tag{B12}$$

$$\overline{V}_p = -\frac{3}{2}\Omega_0 x - \frac{(1+\epsilon)\eta r_0\Omega_0}{\tau_s^2 + (1+\epsilon)^2}. \tag{B13}$$

This paper has been typeset from a TEX/LATEX file prepared by the author.